



Order by disorder and an emergent Kosterlitz-Thouless phase in a triangular Rydberg arraySibo Guo ^{1,2,*}, Juntao Huang^{1,2,*}, Jiangping Hu^{1,2,3,†} and Zi-Xiang Li ^{1,2,‡}¹*Beijing National Laboratory for Condensed Matter Physics, and Institute of Physics, Chinese Academy of Sciences, Beijing 100190, China*²*School of Physical Sciences, University of Chinese Academy of Sciences, Beijing 100049, China*³*Kavli Institute for Theoretical Sciences, University of Chinese Academy of Sciences, Beijing 100190, China*

(Received 6 April 2023; accepted 2 August 2023; published 13 November 2023)

A programmable quantum simulator using Rydberg-atom array provides a promising route to demystifying quantum many-body physics in strongly correlated systems. Motivated by the recent realization of various quantum magnetic phases on the frustrated Rydberg-atom array, we perform numerically exact quantum Monte Carlo simulations to investigate the exotic states of matter emerging in the model describing the Rydberg atom on a triangular lattice. Our state-of-the-art simulation unveils the $\sqrt{3} \times \sqrt{3}$ triangular antiferromagnetic order exists at 1/3 or 2/3-Rydberg filling, consistent with the observation in experiments. Remarkably, $\sqrt{3} \times \sqrt{3}$ long-range order arising from order-by-disorder mechanism emerges at 1/2 filling. At finite temperature, U(1) symmetry is emergent at 1/2 filling and a Kosterlitz-Thouless phase transition occurs with increasing temperature. These intriguing phenomena are potentially detected in future Rydberg-atom experiments.

DOI: [10.1103/PhysRevA.108.053314](https://doi.org/10.1103/PhysRevA.108.053314)**I. INTRODUCTION**

Deciphering the exotic physics emerging in frustrated magnets is a particularly intriguing and crucial subject in strongly correlated physics, triggering enduring interests for many years [1,2]. In light of recent experimental developments, the models featuring quantum magnetism in the presence of lattice frustration are realized in Rydberg atom arrays [3–5]. In light of the high controllability and precise measurability in the Rydberg atom set-up [6–19], fruitful exotic phenomena emerging in frustrated magnets, including various spin density wave orders, and quantum spin liquid have been observed in the platform of the Rydberg atom array [3–5,20–29]. Hence, the Rydberg atom array provides an ideal candidate platform for quantum simulation on quantum magnetism [26,27,30–55] and other exotic phenomena in strongly correlated systems [28,56–77].

The triangular Ising model with transverse field is a representative model featuring quantum magnetism with lattice frustration. Despite its simple form, the triangular transverse Ising model is theoretically revealed to exhibit various intriguing phenomena arising from the interplay between lattice frustration and quantum or thermal fluctuations. For example, quantum fluctuation triggers a $\sqrt{3} \times \sqrt{3}$ ordered phase, emerging from the macroscopic degenerate states induced by the lattice frustration, which is dubbed as the order-by-disorder (OBD) mechanism [78–88]. At finite temperature, there exists an intermediate critical phase with emergent U(1) symmetry, namely the Kosterlitz-Thouless (KT) phase, owing to the interplay of quantum and thermal fluctuations in the

presence of lattice frustration [89–95]. Recently, a Rydberg atom array with up to 196 atoms and high coherence on the triangular lattice was realized experimentally, featuring an Ising-like model involving long-range interactions [3]. Remarkably, the classical pattern of $\sqrt{3} \times \sqrt{3}$ antiferromagnetic (AFM) order is observed. Nevertheless, the realization of OBD phase and associated intriguing physics such as the emergent U(1) symmetry in the Rydberg atom's platform remains elusive. A thorough study of the systems with numerically exact theoretical approach, rigorously illustrating the plausibility of realization of the exotic physics discussed above in the triangular Rydberg atom array, is thus immensely desired.

In this paper, we perform numerically exact quantum Monte Carlo (QMC) simulation based on a stochastic series expansion (SSE) [89,96,97] algorithm to investigate a realistic model describing the Rydberg atom array on a triangular lattice [3]. We implement the algorithm combining the line update [98] and multibranch update, enabling studying the model at low temperature and large system size with relatively high efficiency. Our state-of-the-art QMC simulation reveals the existence of $\sqrt{3} \times \sqrt{3}$ triangular antiferromagnetic (TAF) order at 1/3 and 2/3 filling, consistent with the observation in experiments. More remarkably, our study demonstrates the emergence of OBD driven $\sqrt{3} \times \sqrt{3}$ ordered phase at 1/2 filling. With increasing temperature, the TAF ordered phases at 1/3 and 2/3 filling melt into disordered phase through a continuous transition belonging to two-dimensional Potts universality class. Intriguingly, at 1/2 filling, the U(1) isotropy emerges in a large temperature regime and the associated transition from the OBD phase to high-temperature disordered phase thus belongs to the KT universality class [99]. Our study paves an alternative avenue to theoretically investigate the Rydberg atom array system in a numerically exact approach. The results provide concrete theoretical support to potentially

*These authors contributed equally to this work.

†Corresponding author: jphu@iphy.ac.cn‡Corresponding author: zixiangli@iphy.ac.cn

realizing the exotic phenomena, for instance, the OBD phase, emergent U(1) symmetry, and KT phase transition, in the Rydberg atom platform.

II. MODEL AND METHOD

We consider the following Hamiltonian describing the two-dimensional (2D) interacting Rydberg array [3]:

$$\hat{H} = \sum_{i<j} U_{ij} \hat{n}_i \hat{n}_j + \frac{\hbar\Omega}{2} \sum_i (\hat{b}_i^\dagger + \hat{b}_i) - \hbar\delta \sum_i \hat{n}_i, \quad (1)$$

where \hbar is the reduced Planck's constant, Ω is the Rabi frequency, δ is the detuning frequency, and \hat{n}_i denotes Rydberg occupation on site i . The model features a long-range van der Waals interaction between Rydberg atoms $U_{ij} = \Omega(R_b/r_{ij})^6$, where R_b is the Rydberg blocking radius defined as $U_{ij} = \Omega$ if $r_{ij} = R_b$. We investigate Eq. (1) on the triangular lattice with the lattice basis vectors $\vec{a}_1 = a(1, 0)$ and $\vec{a}_2 = a(\frac{1}{2}, \frac{\sqrt{3}}{2})$. Unless specified, we choose $\hbar = 1$ and $\Omega = 1$ in the simulation.

Upon fixing R_b , with the increase of detuning frequency δ , atoms in the ground state are gradually excited to the Rydberg state, exhibiting various patterns in real space with different average Rydberg fillings [3,34,35]. In particular, as the blockade radius is comparable to the lattice constant on a triangular lattice, namely, $a \leq R_b \leq \sqrt{3}a$, the Rydberg atoms form an incompressible TAF pattern with $\sqrt{3} \times \sqrt{3}$ periodicity as revealed in Ref. [3]. In this study, we fix the blockade radius $R_b = 1.2a$ and select the system size $L_x = L_y = L$ with periodic boundary condition. Owing to the absence of a sign problem [98,100–104], the accurate properties of Eq. (1) for large system size and low temperature are accessible in QMC simulation. The details of QMC simulation and the results of other choices of R_b such as $R_b = 1.0a$ are included in Appendixes A and C.

III. PHASE DIAGRAM

We calculate the average Rydberg filling \bar{n} at zero temperature versus δ as depicted in Fig. 1, showing that the Rydberg filling gradually increases from 0.1 to 1 with increasing δ . The results explicitly indicate that two plateaus appear at 1/3 and 2/3 filling associated with incompressible phases. To further reveal the spontaneous symmetry breaking (SSB) patterns of Rydberg atoms, we calculate the order parameter m and the static structure factor $S(\vec{Q})$ corresponding to the $\sqrt{3} \times \sqrt{3}$ TAF phase, defined as the Fourier transform of the Rydberg occupation \hat{n}_i and the correlation function between \hat{n}_i and \hat{n}_j , respectively,

$$m = \sum_i \langle \hat{n}_i \rangle e^{i\vec{Q} \cdot \vec{x}_i} / (N/3), \quad (2)$$

and

$$S(\vec{Q}) = \frac{1}{N} \sum_{i,j} e^{i\vec{Q} \cdot (\vec{x}_i - \vec{x}_j)} \langle \hat{n}_i \hat{n}_j \rangle. \quad (3)$$

Here, $\vec{Q} = \frac{1}{a}(2\frac{\pi}{3}, 2\frac{\sqrt{3}\pi}{3})$ and N is the total number of lattice points. m and $S(\vec{Q})$ at the thermodynamic limit ($L \rightarrow \infty$) are extracted from the results of $L = 3-18$, the details of which are included in Appendix B. As depicted in Figs. 2(a) and

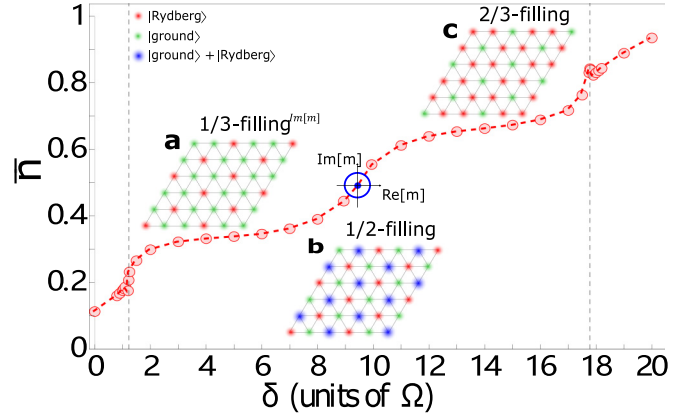


FIG. 1. Average Rydberg filling. The red dots connected by the dashed line represent the Rydberg filling versus δ in Eq. (1). Insets (a) to (c) show the patterns of TAF order at 1/3, 1/2, and 2/3 filling, respectively. The blue circle represents the distribution of TAF order parameters at 1/2 filling, which indicates the appearance of U(1) symmetry.

2(b), $|m|$ and $S(\vec{Q})$ are finite at the thermodynamic limit in a large regime of δ , indicating the existence of $\sqrt{3} \times \sqrt{3}$ TAF long-range order. Both of these quantities exhibit the feature of pronounced convexity in the regime corresponding to the 1/3 or 2/3 filling platform in Fig. 1, suggesting the ground state of Eq. (1) possesses strong $\sqrt{3} \times \sqrt{3}$ TAF long-range order at the commensurate 1/3 and 2/3 filling, consistent with the observation in Rydberg atom array experiments [3]. With increasing δ , the results of $|m|$ and $S(\vec{Q})$ display sharp discontinuous transitions around $\delta_c \approx 1.2$ and 17.8, signaling the nature of the first-order transition between disordered and TAF phases.

To further corroborate the emergence of $\sqrt{3} \times \sqrt{3}$ TAF long-range order and determine the accurate transition point,

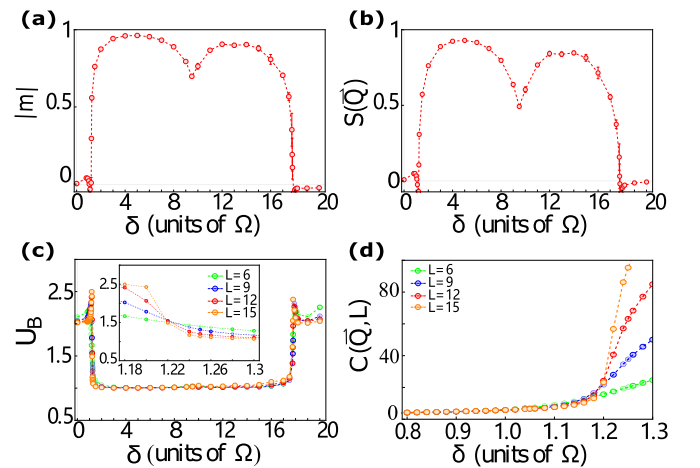


FIG. 2. Ground-state phase diagram and transition point. (a), (b) represent the results of order parameter and static structure factor versus δ at the thermodynamic limit, respectively. (c) Binder ratio versus δ for $L = 6, 9, 12, 15$. The inset provides a zoomed-in view of U_B in the regime close to the transition point. (d) Correlation length ratio versus δ in the regime close to the transition point.

we perform finite-size scaling analysis by calculating the Binder ratio [34,105–107] defined as $U_B(L) = \frac{\langle |m|^4 \rangle}{\langle |m|^2 \rangle^2}$. In the long (short)-range ordered phase, the values of $U_B(L)$ should decrease (increase) with increasing system size L and tend to 1 (2) in the thermodynamic limit. Figure 2(c) shows the results of U_B versus δ and the nearly crossing point from different sizes L indicates the phase transition occurring at $\delta/\Omega = 1.22 \pm 0.02$, in agreement with the results of $|m|$ and $S(\vec{Q})$. The nonmonotonic behavior of $U_B(L)$ close to the phase transition point manifests the nature of first-order transition. Additionally, we calculate the correlation length ratio [35,97] defined as $C(\vec{Q}, L) = \frac{S(\vec{Q})}{S(\vec{Q} + \vec{\delta}_q)}$, where $\vec{Q} + \vec{\delta}_q$ is the momentum closest to \vec{Q} on the lattice. As depicted in Fig. 2(d), the results of $C(\vec{Q}, L)$ for different system sizes reveal the transition from disordered to TAF phase occurs at $\delta_{c1} \approx 1.2$. Similarly, $U_B(L)$ and $C(\vec{Q}, L)$ yield another phase boundary between the TAF and disordered phases $\delta_{c2} \approx 17.8$. Taken together, our systematic numerical simulations utilizing various approaches unambiguously establish the ground-state phase diagram of Rydberg atoms on a triangular lattice as presented in Figs. 1 and 2. Notice that the ground-state phase diagram does not qualitatively change with respect to slightly varying the value of R_b , as suggested by the numerical results of $R_b = 1.0a$ included in Appendix C.

IV. OBD AT 1/2 FILLING

The $\sqrt{3} \times \sqrt{3}$ TAF phases at 1/3 or 2/3 filling established in our state-of-the-art numerical simulation are consistent with recent experimental observations [3]. An intriguing question is whether the $\sqrt{3} \times \sqrt{3}$ TAF order could emerge at 1/2 filling, arising from the celebrated OBD mechanism as developed in the triangular quantum transverse-field Ising model [78–82]. In Figs. 2(a) and 2(b), the finite order parameter and structure factors at the thermodynamic limit demonstrate the presence of $\sqrt{3} \times \sqrt{3}$ TAF long-range order at 1/2 filling. Furthermore, the results of the Binder ratio in Fig. 2(c) rigorously confirm the conclusion. The explicit results of order parameters, structure factors, and Binder or correlation length ratios at 1/2 filling for different system sizes are included in Appendix B.

V. KT PHASE WITH U(1) SYMMETRY

From the perspective of symmetry, the TAF phase at 1/3 or 2/3 filling breaks the Z_3 lattice translational (or rotational) symmetry. At 1/2 filling, the system accommodates an extra Z_2 particle-hole symmetry, namely, the ground state of the TAF phase is six-fold degenerate. Hence, the resulting Landau free-energy characterizing TAF ordering is written as

$$F \propto g_2 |m|^2 + g_4 |m|^4 + \begin{cases} g_3 |m|^3 \cos 3\theta, & \text{for 1/3 and 2/3 filling,} \\ g_6 |m|^6 \cos 6\theta, & \text{for 1/2 filling,} \end{cases} \quad (4)$$

where $|m|$ and θ represent the modulus and phase of the order parameter in Eq. (2), $g_{2,3,4,6}$ are the coefficients of each term, and $|m|^3 \cos 3\theta$ and $|m|^6 \cos 6\theta$ are known as the three- and six-fold anisotropic terms breaking the U(1) symmetry of

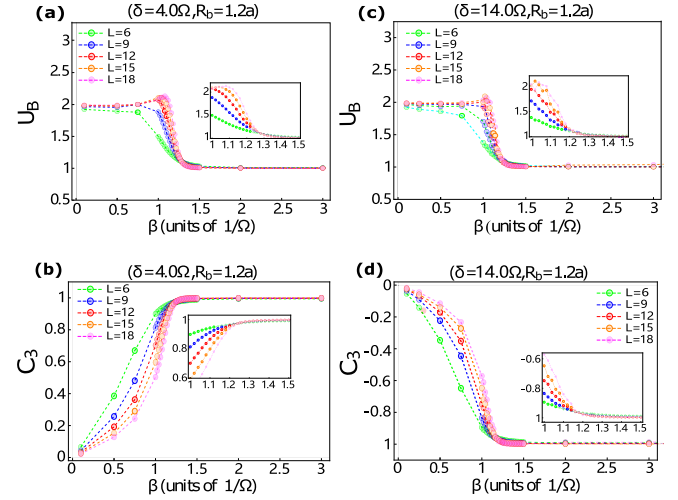


FIG. 3. Transition of TAF phase at finite temperature. (a), (c) represent the results for Binder ratio as a function of β at 1/3 and 2/3 filling, respectively. (b), (d) represent the results for C_3 as a function of β at 1/3 and 2/3 filling, respectively. The system sizes in the simulation are $L = 6, 9, 12, 15, 18$. The insets provide a zoomed-in view in the regime close to the transition point.

m down to Z_3 and Z_6 [107,108], respectively. For the TAF ordered to disorder transition in a two-dimensional system at finite temperature, the Z_3 anisotropic term is relevant, resulting in the phase transition belonging to the three-state Potts universality class [106]. However, Z_6 anisotropy is presumably irrelevant in the presence of strong thermal fluctuation, yielding an intermediate phase with the emergent U(1) isotropy of the TAF order parameter, namely, a KT phase [82]. The phase transition between the quasi-long-range KT phase and the disordered phase at higher temperature belongs to the celebrated KT universality class [109,110]. Thus, to further elaborate on the nature of TAF ordered phases at 1/3 or 2/3 and 1/2 filling, we embark on investigating the SSB and associated phase transitions at finite temperature.

To explicitly characterize the anisotropy in the $\sqrt{3} \times \sqrt{3}$ TAF phases, we calculate the following quantity:

$$C_q = \frac{\langle |m|^q \cos q\theta \rangle}{\langle |m|^q \rangle}, \quad q = 3, 6, \quad (5)$$

which is finite in the phase featuring three- or six-fold anisotropy [106,107]. If the Z_q anisotropic term is irrelevant, namely, the ground-state manifold is a U(1) group, such a quantity is expected to vanish at the thermodynamic limit. In addition, we also calculate the Binder ratio to identify transition points at finite temperature, which are presented together with C_3 in Fig. 3. The crossing feature of the Binder ratio with varying system sizes in Figs. 3(a) and 3(c) clearly demonstrate a finite-temperature transition from TAF phase to disordered phase, where the critical temperature at 1/3 and 2/3 filling are $\beta_c \Omega = 1.28 \pm 0.02$ and 1.22 ± 0.02 , respectively. In the TAF phase at $\beta > \beta_c$ shown in Figs. 3(b) and 3(d), $|C_3|$ increases with system size, revealing the nature of the anisotropy breaking U(1) symmetry at 1/3 and 2/3 filling. The transition points identified from the crossing point of

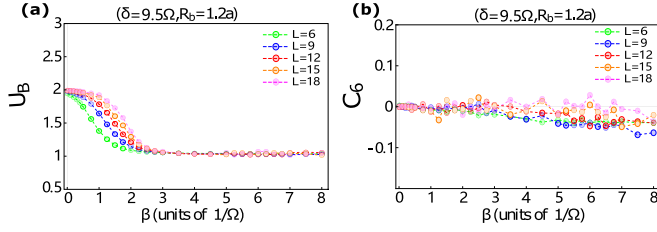


FIG. 4. Irrelevance of sixfold anisotropy. (a), (b) represent Binder ratio and C_6 for parameters $\delta = 9.5\Omega$ corresponding to the $1/2$ filling of Rydberg occupancy. The system sizes in the simulation are $L = 6, 9, 12, 15, 18$.

C_3 for different systems sizes are nearly consistent with the value determined by the Binder ratio. Moreover, we perform a systematic finite-size scaling analysis in Appendix B yielding the accurate critical exponents of the transition, which convincingly verifies the transition in Fig. 3 belongs to the Potts universality class. In contrast, at $1/2$ filling, six-fold anisotropy C_6 vanishes with increasing system size in a large temperature regime indicated in Fig. 4(b), which implies the emergence of U(1) symmetry. In the results of the Binder ratio in Fig. 4(a), the crossing point is not explicitly detected, consistent with the absence of a long-range-order breaking continuous phase transition at finite temperature in two dimensions. The irrelevance of Z_6 anisotropy persists down to the lowest temperature accessible in our simulation $\beta = 150/\Omega$.

To further confirm the emergence of U(1) symmetry in the TAF phase arising from the OBD mechanism at $1/2$ filling, we plot the distribution histograms of TAF order parameters in Figs. 5(a) and 5(b). Figure 5(a) is the histogram of m

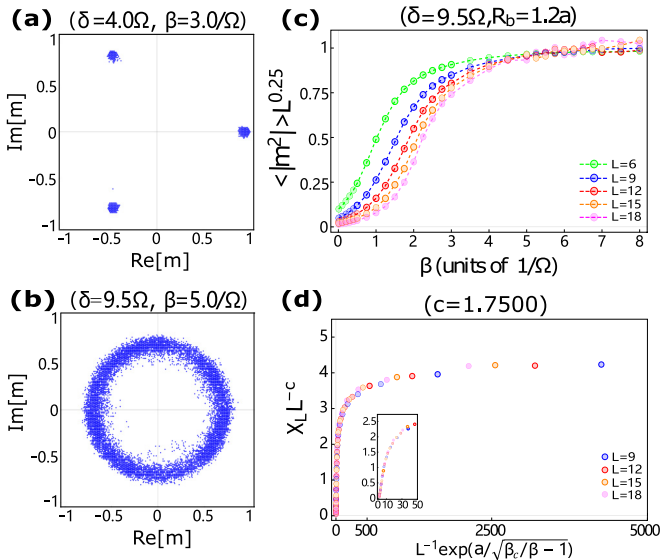


FIG. 5. Histogram of the order parameter and data collapse of the susceptibility. (a,b) represent the distribution histograms of TAF order parameters at $1/3$ and $1/2$ filling of Rydberg occupancy, respectively. (c) The scaled TAF structure factor as a function of β , where the crossing point for different L indicates the KT transition point. (d) shows the finite-size scaling analysis of TAF susceptibility, where the inset in (d) shows the fitting results when $\xi/L \in [0, 50]$.

at $1/3$ filling exhibiting pronounced three-fold anisotropy. It should be noted that the three-fold anisotropy shown in Fig. 5(a) is significantly better than the results in Ref. [3], which is possibly due to the fact that the actual temperature in the experiment is not so exactly the same as that in the numerical simulation. Moreover, the nonequilibrium effect is also a possible factor for this difference. In contrast, as depicted in Fig. 5(b), the distribution histogram of the TAF order parameter at $1/2$ filling is isotropic in the complex plane, providing the unequivocal evidence of the emergent U(1) symmetry. Remarkably, even at $\beta = 150/\Omega$ corresponding to temperature $T = 70$ nK in the Rydberg atom array experiment [3], our calculation in Appendix B reveals that the U(1) symmetry remains present in the histogram of m at $1/2$ filling, manifesting the irrelevance of Z_6 anisotropy at such low temperature.

Furthermore, we decipher the nature of U(1) symmetric TAF phase by investigating the finite-temperature phase transition to the high-temperature disordered phase, belonging to the celebrated KT-transition universality class owing to the emergent continuous U(1) symmetry. Close to the KT-transition point, the susceptibilities of the U(1) order parameters at various system sizes obey the scaling function [99,106,107]

$$\chi_L = L^{2-\eta} \chi_0(\xi/L), \quad (6)$$

where χ_0 is an unknown scaling function, $\xi \propto e^{a/\sqrt{\beta_c/\beta-1}}$ represents the correlation length of the order parameters, displaying divergence at the KT-transition inverse temperature β_c , and a is a nonuniversal constant. The anomalous dimension of order parameter $\eta = 0.25$ exactly holds in the KT transition [82,106,109,110]. We present the results of rescaled susceptibility $\langle |m|^2 \rangle L^{0.25}$ as a function of inverse temperature β in Fig. 5(c), which can be deduced from the order parameter in our simulation through the relation $\chi = L^2 \langle |m|^2 \rangle \beta$, clearly indicating the KT transition occurs at $\beta_c = 6.25/\Omega$ by virtue of the crossing point of rescaled susceptibilities for different system sizes.

Next, we adopt the data collapse analysis of the TAF susceptibility using the scaling function Eq. (6). Assuming KT transition universality class, the data points $(L^{-1} e^{a/\sqrt{\beta_c/\beta-1}}, \chi_L L^{-1.75})$ should collapse into a single curve with appropriate choice of parameters [106,107]. Employing the approach of the data collapse analysis [111,112], we determine the phase transition temperature $\beta_c \Omega = 6.2513 \pm 0.9082$ and $a = 6.5842 \pm 0.9975$, and all data points of each group collapse into a single smooth curve as shown in Fig. 5(d). The estimated value of β_c from data collapse is consistent with the result obtained in Fig. 5(c) within error bar. More crucially, the results of the data collapse provide convincing evidence that the phase transition between the critical KT phase and disordered phases belongs to the KT transition, further verifying the irrelevance of six-fold anisotropy at $1/2$ filling with increasing thermal fluctuation.

VI. CONCLUSION AND DISCUSSIONS

Employing numerically the exact QMC simulation, we systematically investigate a realistic interacting model describing the triangular Rydberg atom array. Upon fixing the

Rydberg radius R_b , the ground-state phase diagram with varying Rydberg filling is achieved. At $1/3$ and $2/3$ filling, the $\sqrt{3} \times \sqrt{3}$ TAF long-range order is unambiguously unveiled, consistent with the observation in recent Rydberg atom array experiments on a triangular lattice [3]. More appealingly, our calculation reveals the $\sqrt{3} \times \sqrt{3}$ ordering is present at $1/2$ filling, arising from the OBD mechanism. Owing to the interplay between quantum and thermal fluctuations, an enlarged $U(1)$ isotropy of the TAF order parameter emerges in a large temperature regime, resulting in a KT transition between the TAF and disordered phases. Since the classical patterns of TAF order at $1/3$ and $2/3$ filling have been successfully imaged in a recent experiment [3], our state-of-the-art numerical simulation paves the route for subsequent observations of quantum fluctuation triggered OBD $\sqrt{3} \times \sqrt{3}$ TAF phase and the intriguing physics including the emergent KT phase and phase transition in the Rydberg atom platform.

We remark that the nonequilibrium effect is a factor that we ignore in the present calculations. To maintain the adiabaticity and reduce the decoherence effect of spontaneous radiation from the intermediate state, a suitable sweep and measurement time are required. In general, the system is considered to be in equilibrium during this time and can be numerically simulated using Eq. (1). The nonequilibrium effect in the Rydberg-atom array is an issue left for our future studies. In addition, it is fascinating to investigate Eq. (1) with further increasing Rydberg blocking radius R_b . As discussed in previous studies, various magnetic ordered phases [34,35], more intriguingly, the quantum spin liquid phase featuring topological order could possibly emerge by using a varying Rydberg blocking radius [5,35]. Moreover, it is straightforward to generalize our study to Rydberg systems in other lattices or modified interactions. Hence, we believe that our study opens an avenue to investigating exotic physics emerging in the Rydberg atom array on a frustrated lattice by using unbiased numerical simulation.

ACKNOWLEDGMENTS

S.G. and J.H. are supported by the Ministry of Science and Technology (Grant No. 2022YFA1403901), the National Natural Science Foundation of China (Grant No. NSFC-11888101), the New Cornerstone Investigator Program, and the Strategic Priority Research Program of the Chinese Academy of Sciences (Grant No. XDB28000000).

APPENDIX A: INTRODUCTION TO SSE QMC

A general introduction to the numerical simulation method (SSE QMC) used in this work is given in this section. In Appendix A1, we show the basic idea of the SSE method at finite temperature applied to the Rydberg system. Then the updated strategy used in the sampling of the simulation cell is shown in Appendix A2, which includes two schemes: the multibranch and line cluster update. Finally, we give the calculation method at zero temperature in Appendix A3.

1. Algorithm of at finite temperature

The SSE QMC is based on Taylor expansion of the physical statistical quantity in the partition function. We consider the Hamiltonian describing the Rydberg atom array, and write the associated partition function in the basis of Rydberg state occupancy as

$$\begin{aligned} Z &= \text{Tr}\{e^{-\beta\hat{H}}\} = \sum_{\psi_0} \langle \psi_0 | \sum_{n=0}^{+\infty} \frac{\beta^n}{n!} (-\hat{H})^n | \psi_0 \rangle \\ &= \sum_{\{\psi_p\}} \sum_{n=0}^{+\infty} \frac{\beta^n}{n!} \prod_{p=1}^n \langle \psi_{p-1} | (-\hat{H}) | \psi_p \rangle. \end{aligned} \quad (\text{A1})$$

In the second equal sign in Eq. (A1), we insert a set of Rydberg basis in every term of the expansion, where $p = 1, \dots, n$ labeling the index related to the imaginary time in path-integral representation. To formulate the SSE QMC more explicitly, we decompose the Hamiltonian as

$$\hat{H} = - \sum_{t,a} \hat{H}_{t,a}, \quad (\text{A2})$$

where the index t represents the diagonal or off-diagonal term in the Rydberg basis, and a represents the index of the lattice site and bond. Substituting Eq. (A2) into Eq. (A1), we arrive at

$$Z = \sum_{\{\psi_p\}} \sum_{n=0}^{+\infty} \sum_{S_n} \frac{\beta^n}{n!} \prod_{p=1}^n \langle \psi_{p-1} | \hat{H}_{t_p, a_p} | \psi_p \rangle, \quad (\text{A3})$$

where $S_n = (t_1, a_1), (t_2, a_2), \dots, (t_n, a_n)$ denotes a sequence of decomposed terms in the Hamiltonian at index n . Practically, we truncate the value of n to a sufficiently large number M . The value of M is determined by the standard procedure as introduced in Refs. [89,98]. Upon the given M , we insert $M - n$ unit operators so that the number of imaginary-time points in each term is fixed to M . Consequently, the partition function Eq. (A3) is expressed as a summation of nonzero weights as

$$\begin{aligned} Z &= \sum_{\{\psi_p\}} \sum_{S_M} \frac{\beta^n (M-n)!}{M!} \prod_{p=1}^M \langle \psi_{p-1} | \hat{H}_{t_p, a_p} | \psi_p \rangle \\ &= \sum_{\{\psi_p\}} \sum_{S_M} \Psi(\{\psi_p\}, S_M). \end{aligned} \quad (\text{A4})$$

In QMC simulation, we perform the summation in Eq. (A4) stochastically, more explicitly, we sample the configuration space $(\{\psi_p\}, S_M)$ randomly with the probability $\Psi(\{\psi_p\}, S_M)$ defined in Eq. (A4). Then some physical observables can be evaluated straightforwardly. For example, the energy could be calculated as following:

$$E = \langle \hat{H} \rangle = \frac{1}{Z} \text{Tr}\{\hat{H} e^{-\beta\hat{H}}\} = \frac{1}{Z} \sum_{n=1}^{+\infty} \frac{\beta^n n}{n! \beta} \text{Tr}\{-\hat{H}^n\} = -\frac{\langle n \rangle}{\beta}. \quad (\text{A5})$$

So the energy in the thermal equilibrium corresponds to the average value of n divided by inverse temperature β . In the SSE QMC simulation, the diagonal update is adopted to insert or delete the site or bond diagonal operator, which keeps the configuration of states $\{\psi_p\}$ at each imaginary time invariant.

The off-diagonal update inserts or deletes the off-diagonal site operator, hence updating the configuration $\{\psi_p\}$. The cluster algorithm is utilized to achieve it efficiently.

To guarantee the absence of the sign problem in the procedure of SSE QMC simulation, the matrix elements in Eq. (A4) should be nonnegative. Under a unitary transformation $\hat{U} = \bigotimes_{i=1}^N \hat{n}_i^z$, the Hamiltonian is transformed as

$$\hat{H} = \sum_{i<j} U_{ij} \hat{n}_i \hat{n}_j - \frac{\Omega}{2} \sum_i (\hat{b}_i^\dagger + \hat{b}_i) - \delta \sum_i \hat{n}_i. \quad (\text{A6})$$

Then we decompose the above Hamiltonian into the following components:

$$\begin{aligned} \hat{H}_{0,0} &= \hat{I}, \quad \hat{H}_{0,a} = \frac{\Omega}{2} \hat{I}, \quad \hat{H}_{-1,a} = \frac{\Omega}{2} \hat{\sigma}_i^x, \\ \hat{H}_{1,b} &= -U_{ij} \hat{n}_i \hat{n}_j + \delta_b (\hat{n}_i + \hat{n}_j) + C_{ij}, \end{aligned} \quad (\text{A7})$$

where $\delta_b = \frac{\delta}{N-1}$ and the constant $C_{ij} = |\min(0, \delta_b, 2\delta_b - U_{ij})|$ is added to eliminate the sign problem. The first indexes 0, 1, and -1 represent the unit, diagonal, and off-diagonal operators, respectively, while the second indexes a and b correspond to operators on the lattice site and bond. Here, we list the nonzero matrix elements of each component in Eq. (A7) as follows:

$$\begin{aligned} \langle 1 | \hat{H}_{-1,a} | 0 \rangle &= \langle 0 | \hat{H}_{-1,a} | 1 \rangle = \frac{\Omega}{2}, \\ \langle 1 | \hat{H}_{1,a} | 1 \rangle &= \langle 0 | \hat{H}_{1,a} | 0 \rangle = \frac{\Omega}{2}, \\ G_{ij}^{(1)} &\equiv \langle 00 | \hat{H}_{1,b} | 00 \rangle = C_{ij}, \\ G_{ij}^{(2)} &\equiv \langle 01 | \hat{H}_{1,b} | 01 \rangle = \delta_b + C_{ij}, \\ G_{ij}^{(3)} &\equiv \langle 10 | \hat{H}_{1,b} | 10 \rangle = \delta_b + C_{ij}, \\ G_{ij}^{(4)} &\equiv \langle 11 | \hat{H}_{1,b} | 11 \rangle = -U_{ij} + 2\delta_b + C_{ij}, \end{aligned} \quad (\text{A8})$$

where G_{ij} represents the matrix element on the bond ij . The key procedure in the QMC simulation updates the configurations efficiently. Hence, we introduce the update strategy in the SSE QMC simulation on the Rydberg atom array system in the next section.

2. Update strategy

The update of configurations in the imaginary-time direction is divided into two steps: diagonal and off-diagonal update, discussed in Appendixes A 2 a and A 2 b, respectively.

a. Diagonal update

The first class of update scheme in SSE QMC simulation is the diagonal update. In the diagonal update, the diagonal terms in the Hamiltonian are inserted or replaced by the unit operator. The configurations of states at each imaginary time, namely, $\{\psi_p\}$, thus keep invariant in the procedure of the diagonal update. The procedure of the diagonal update in our simulation is similar to the algorithm utilized in the long-range Ising model.

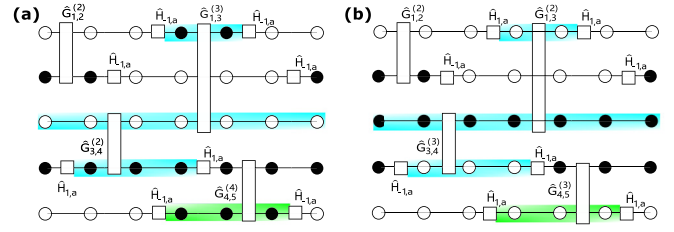


FIG. 6. (a), (b) show the simulation cells before and after the off-diagonal update. The hollow and solid circles represent the ground-state and Rydberg atoms on the lattice point, respectively, and the blue and green paths represent the cluster used for multibranch and line update, respectively.

b. Off-diagonal update

For the off-diagonal operator update, the multibranch cluster algorithm is proposed to efficiently update the configurations in the long-range Ising model. For the Rydberg system, Melko *et al.* [98] proposed a line update algorithm. The line update is a cluster update algorithm local in space and nonlocal in imaginary time. Unlike the multibranch update in which all the four legs in the bond operator are added in the cluster, in the line cluster, only the neighbored leg in the imaginary-time direction is added to the cluster when the bond operator is encountered. The advantage of the line update in Rydberg systems over the multibranch update is that the first can sample more configurations than the second, which can better meet the ergodic requirements. However, the multibranch update process enables updating the configurations in a cluster containing different sites. Thus, we perform the off-diagonal update combining two schemes of the line update and multibranch update.

Here, to further understand this update strategy, we take the concrete example shown in Fig. 6, where the x and y directions represent the imaginary-time direction and the arrangement of lattice points in real space, respectively. The clusters corresponding to the blue and green paths in Fig. 6(b) are the updated configurations of the clusters with the corresponding colors in Fig. 6(a), where the blue and green correspond to the multibranch and line update strategies, respectively. As we can see, in the multibranch update, all four legs of the bond operator encountered by the blue path are added to the cluster, while only the two adjacent legs of the green path in the line update are taken into account.

3. Method of accessing zero-temperature information

In the two subsections above, we introduced the numerical methods used for the simulation at finite temperature. To access the ground-state properties of the Rydberg-atom systems, we perform the finite-temperature simulation and scale the inverse temperature linearly with system size as $\beta = 2L$. Then the results at zero temperature are extrapolated from the data for different system sizes L and inverse temperatures β through the second polynomial function

$$y = a \left(\frac{1}{L} \right)^2 + b \left(\frac{1}{L} \right) + c, \quad (\text{A9})$$

where y is the extrapolated result for zero temperature and a, b, c are nonuniversal parameters in the fitting. Employing

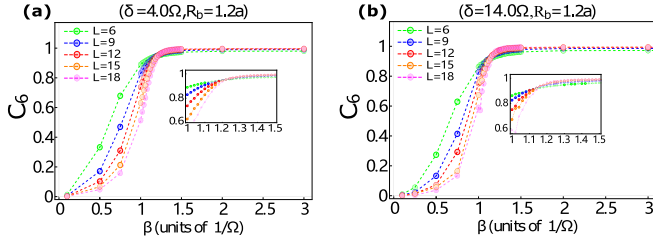


FIG. 7. (a), (b) represent the results of C_6 for parameters $\delta = 4.0\Omega$ and 14.0Ω corresponding to the Rydberg 1/3 and 2/3 filling, respectively. Here, five different system sizes are used for finite-size scaling analysis, marked by different colors in the legend. The insets in (a) and (b) also show the trend near the phase transition and give the specific position of the transition points.

this procedure, we achieve the results of different physical quantities at the thermodynamic limit and zero-temperature limit, namely, $L \rightarrow \infty$ and $T \rightarrow 0$.

APPENDIX B: ADDITIONAL NUMERICAL RESULTS FOR $R_b = 1.2a$

In this section, we provide more numerical results with $R_b = 1.2a$, further confirming the conclusions in the main text. In Appendix B 1, we present the results of finite-size scaling analysis for the TAF disordered phase transition at 1/3 and 2/3 filling. In Appendix B 2, we present the distribution histograms of order parameters at varying temperatures. Remarkably, the KT phase emerging at 1/2 filling exists in a large temperature regime, persisting down to the temperature close to zero temperature. In Appendix B 3, we present the results for the filling of Rydberg occupancy slightly away from 1/2, demonstrating that the KT phase only exists at 1/2

filling. Finally, in Appendix B 4, we determine the critical temperature of the KT transition by data collapse with the data adding $L = 6a$, which renders the results qualitatively consistent with the ones in the main text. Moreover, we perform double logarithmic fitting of TAF susceptibility, giving rise to the KT-transition temperature consistent with the result obtained by data collapse.

1. Finite-temperature Potts transition at 1/3 and 2/3 filling

In this subsection, by further calculating C_6 , which represents the six-fold anisotropy, we give the transition points in Fig. 3 in the main text again. Then a finite-size scaling analysis is carried out to demonstrate that the phase transition in Fig. 3 belongs to the Potts universality class.

First, for Fig. 3 in the main text, C_3 is calculated to characterize the three-fold anisotropy at 1/3 and 2/3 filling and give the transition points, which is consistent with the results from the Binder ratio. In fact, similar results can also be obtained by C_6 . Figure 7 shows the results of C_6 with parameters $\delta = 4.0\Omega$ and 14.0Ω , from which we can see that the critical temperatures between the 1/3- and 2/3-filling phase and disordered phase are $\beta_c\Omega = 1.22 \pm 0.02$ and 1.16 ± 0.02 , respectively. By comparing Figs. 3 and 7, it can be seen that C_3 is indeed more accurate than C_6 in characterizing the three-fold anisotropy of TAF order at 1/3 and 2/3 filling.

Then, at 1/3 and 2/3 filling, here we also perform a finite-size scaling analysis for the susceptibility χ_L at finite temperature, where χ_L of different sizes follows

$$\chi_L = L^c \chi_0(L/\xi), \quad (\text{B1})$$

Eq. (B1) has a similar form to Eq. (6) in the main text, and the correlation length $\xi \propto 1/(\beta - \beta_c)^{\nu}$, where the theoretical

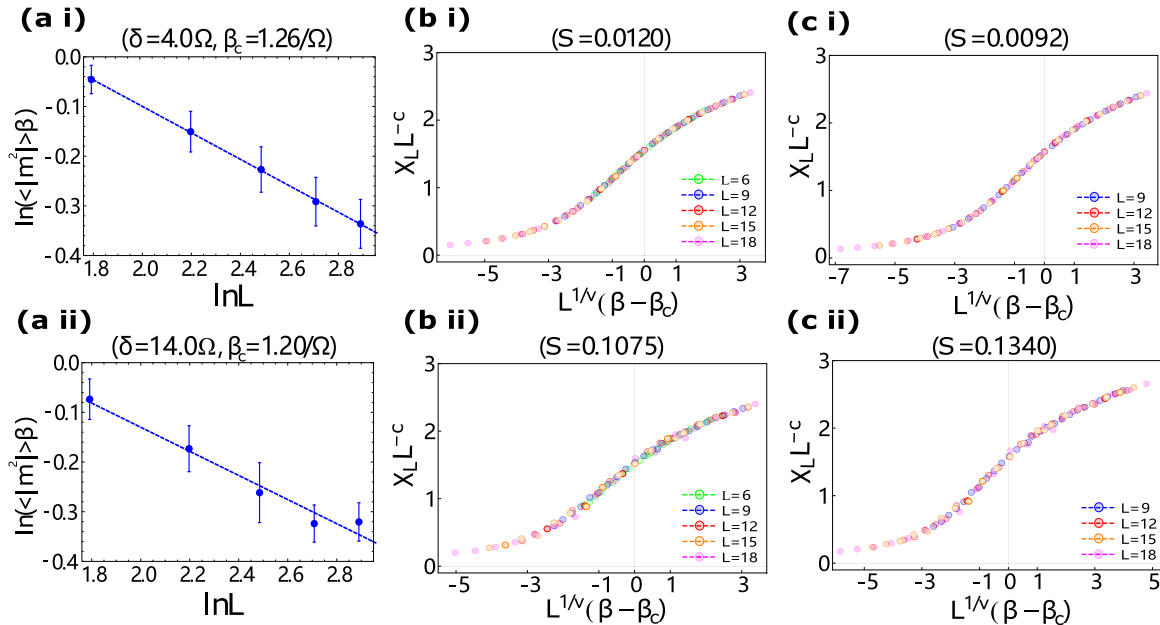


FIG. 8. The first and second rows correspond to the fitting results of 1/3 and 2/3 filling, respectively. The first column shows the double logarithm fitting in Eq. (B4) at the transition temperature β_c . The second and third columns give the results of data collapse analysis for system sizes $L/a = 6, 9, 12, 15, 18$ and $9, 12, 15, 18$, respectively, where different colors in the legend represent different sizes.

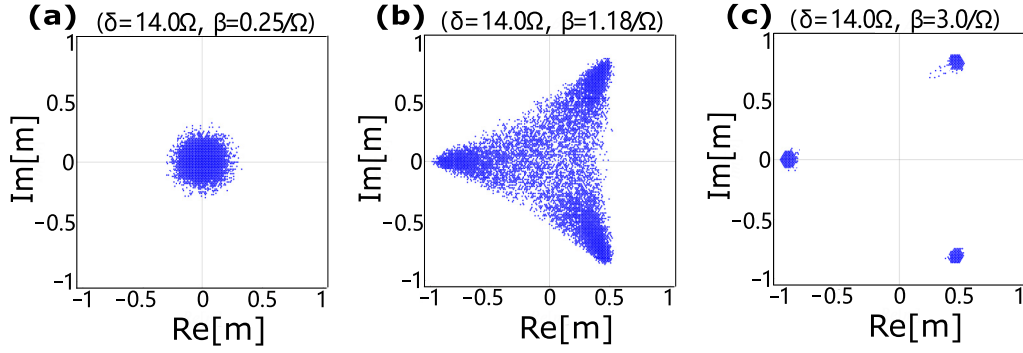


FIG. 9. (a)–(c) show the distribution histograms of order parameters with 14.0Ω at three representative temperatures, which reflects the phase transition from disordered phase to TAF phase at $2/3$ filling.

value of the Potts universality class is

$$c = \frac{26}{15}, \quad \nu = \frac{5}{6}. \quad (\text{B2})$$

At the transition temperature β_c , the susceptibility can be reduced to

$$\chi_L \propto L^c. \quad (\text{B3})$$

Taking the logarithm of both sides of Eq. (B3), we can obtain

$$\ln(\langle |m|^2 \rangle \beta) = \ln \alpha - (2 - c) \ln L, \quad (\text{B4})$$

where α is a constant coefficient. Equation (B4) is used to fit anomalous dimension c at different temperatures. As shown in Fig. 8(a), it can be seen that for $1/3$ and $2/3$ filling, the anomalous dimension at $\beta_c \Omega = 1.26$ and 1.20 and $c =$

1.7337 ± 0.00029 and 1.7573 ± 0.0248 , respectively, which are in good agreement with the theoretical values in Eq. (B2).

Further, according to Eq. (B1), we perform a data collapse analysis, that is, $[L^{1/\nu}(\beta - \beta_c), \chi_L L^{-c}]$ should collapse into a common curve, which is similar to the result Fig. 5(d) in the main text. From the fitting results of Figs. 8(b i) to 8(b ii) corresponding to $1/3$ and $2/3$ filling, respectively, where the system size is selected as $L/a = 6, 9, 12, 15, 18$, we obtain that the fitting parameters are $(c, \nu, \beta_c) = (1.7305 \pm 0.1622, 0.8706 \pm 0.0124, 1.2597 \pm 0.0502)$ and $(1.7267 \pm 0.1508, 0.8672 \pm 0.0244, 1.1993 \pm 0.0157)$.

Compared with Fig. 8(b), we also give the fitting of system size $L/a = 9, 12, 15, 18$ in Fig. 8(c), and the obtained results are $(c, \nu, \beta_c) = (1.7263 \pm 0.1462, 0.8632 \pm 0.0102, 1.2596 \pm 0.0184)$ and $(1.7125 \pm 0.1092, 0.8536 \pm$

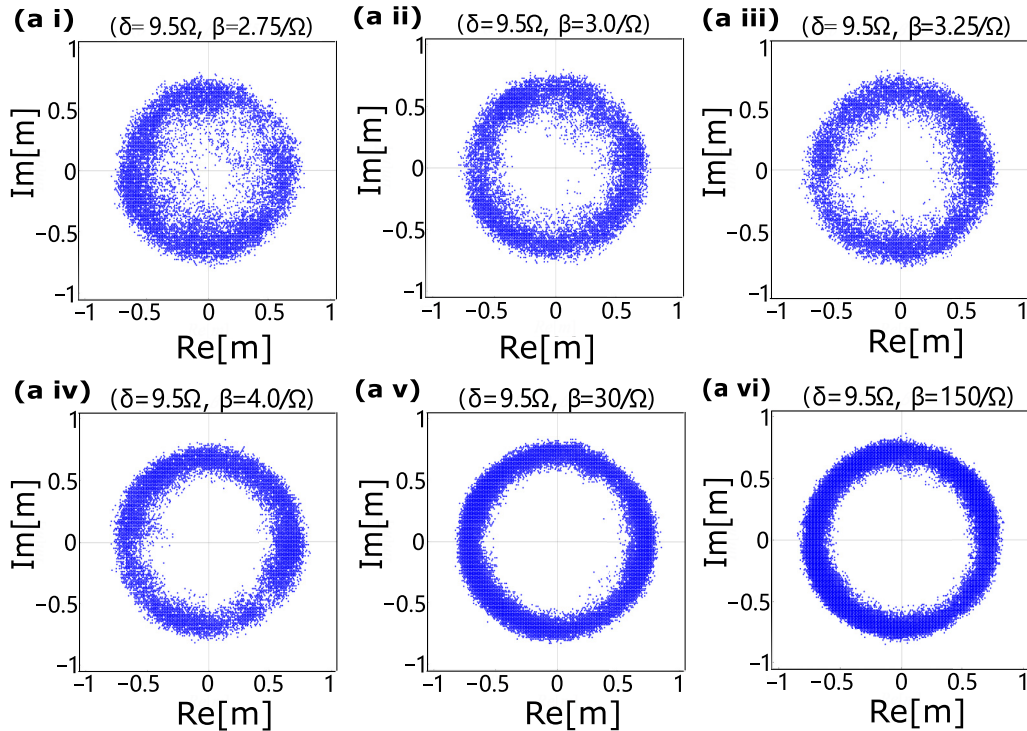


FIG. 10. The six figures are the distribution histograms of TAF order parameters with $\delta = 9.5\Omega$ at different temperatures, where the corresponding temperatures in Rydberg-atom array experiment of (a v) and (a vi) are 350 nK and 70 nK, respectively. With the decrease of temperature, the feature of emergent $U(1)$ isotropy in distribution histogram is more pronounced.

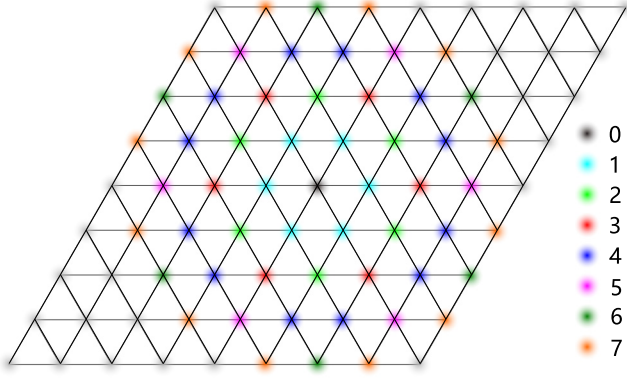


FIG. 11. Each dot represents an atom. Using the black atom labeled 0 as a reference, this figure shows the distribution of atoms around it from the first nearest neighbor to the seventh nearest neighbor, where the corresponding color of the number i represents the i th nearest-neighbor atom and gray represents the more distant atoms beyond the seventh nearest-neighbor position.

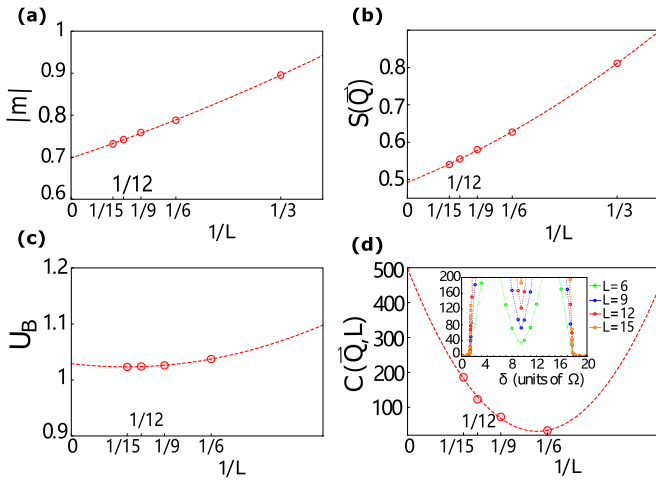


FIG. 12. (a)–(d) show the order parameter m , static structure factor $S(\vec{Q})$, Binder ratio $U_B(L)$, and correlation length ratio $C(\vec{Q}, L)$ corresponding to $\delta = 9.50\Omega$ at $1/2$ filling, respectively, in which the red dotted line in each figure represents the quadratic fitting curve in Eq. (A9) obtained with different data points. The inset in (d) gives the overall trend of $C(\vec{Q}, L)$ when $\delta/\Omega \in [0, 20]$, where $C(\vec{Q}, L)$ at $1/2$ filling is also a local minimum, and five sizes are selected for finite-size scaling analysis and marked with different colors in the legend.

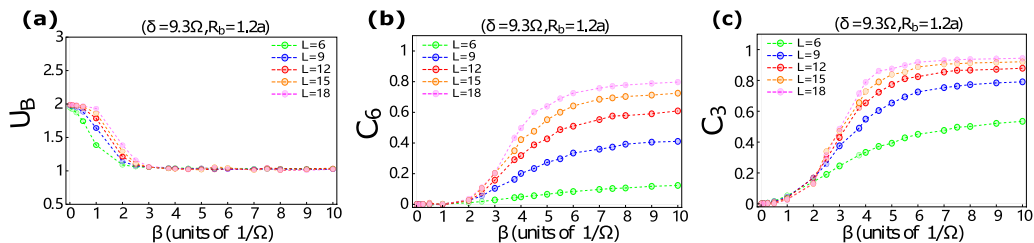


FIG. 13. The results of finite-temperature phase transition for $\delta = 9.3\Omega$. (a) Binder ratio U_B . (b) Six-fold anisotropy C_6 . (c) Three-fold anisotropy C_3 . The system sizes in the simulation are $L/a = 6, 9, 12, 15, 18$.

0.0107, 1.1975 ± 0.0124), respectively. These numerical results in Fig. 8 are consistent with the theoretical values of the Potts transitions in Eq. (B2).

Here we use the fitting method given in Ref. [111], which is a refinement on the method previously proposed in Ref. [112]. In this method, a function S is defined to evaluate the quality of the fitting, where the minimum value is close to 1.0 if the collapse effect is good, otherwise it is a large value. In the fitting of the four data collapses in Fig. 8, the functions obtained are $S = 0.0120, 0.1075, 0.0092$, and 0.1340 , corresponding to Figs. 8(b i), 8(b ii), 8(c i), and 8(c ii), respectively, and these data points of different sizes do collapse onto a common smooth curve. Therefore, from the results of Fig. 8, we can conclude that the TAF disorder transitions for $1/3$ and $2/3$ filling at finite temperature belong to the Potts universality class.

In addition, the distribution histogram of order parameters at $1/3$ filling is given in Fig. 5(a) in the main text. Here we also show the histograms with $\delta = 14.0\Omega$ corresponding to $2/3$ filling in Fig. 9, and it can be seen that the distribution of order parameters still has a three-fold symmetry. The difference between these two filling phases is that the peaks of the phases in Fig. 9(c) are concentrated in $\pi/3, \pi, 5\pi/3$, rather than $0, 2\pi/3, 4\pi/3$ shown in Fig. 5(a) in the main text, which was measured in the experiment [3].

2. KT phase at low temperature

The results of Fig. 4 in the main text illustrate that at $1/2$ filling, with decreasing temperature, the system undergoes a KT transition from the disordered phase to a KT phase with the emergent $U(1)$ isotropy of the TAF order parameter. In the main text, we present the distribution histogram of the TAF order parameter at $1/2$ filling for inverse temperature $\beta = 5.0/\Omega$, corresponding to the temperature in the Rydberg atom array experiment $T = 2.1 \mu\text{K}$ [3]. In this section, we plot the distribution histograms of the TAF order parameters with the size $L = 15a$ at different temperatures, as shown in Fig. 10. With the decrease of temperature, the distribution of order parameters gradually evolves to an isotropic circle. In particular, in Fig. 10(a vi) with the inverse temperature $\beta = 150/\Omega$ corresponding to 70 nK [3] in the experiment, which is extremely close to zero temperature, the result clearly shows that the distribution peaks in a circle with $U(1)$ isotropy. Therefore, $U(1)$ isotropy of the TAF order parameter is emergent in a large-temperature regime, corroborating the feasibility of observing the emergent KT phase in realistic Rydberg atom array experiments. More appealingly, our numerical results

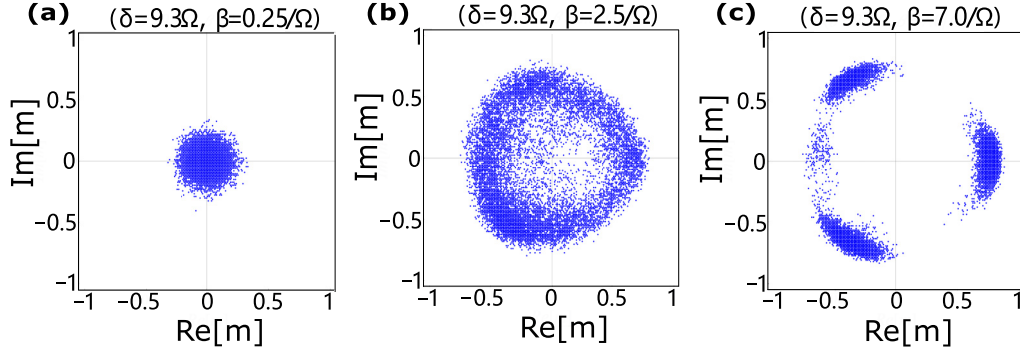


FIG. 14. (a)–(c) show the distribution histograms of order parameters with $\delta = 9.30\Omega$ at three representative temperatures, respectively, which reflects the phase transition from disordered phase to TAF phase.

imply the KT phase with emergent U(1) isotropy persists even to the zero temperature, which is fundamentally different from the transverse-field Ising model with the nearest-neighbor interaction, where the KT phase only emerges in an intermediate temperature regime. The thorough investigation of the possible emergent KT phase at zero temperature is left for future study.

3. Results for the slight deviation from 1/2 filling

In this subsection, we explicitly show that the parameter $\delta = 9.5\Omega$ indeed corresponds to 1/2 filling, consistent with the numerical results presented in the main text. Then we present the numerical results for the Rydberg occupancy slightly away from 1/2 filling, specifically, $\delta = 9.3\Omega$, which demonstrates the KT phase with emergent U(1) symmetry only exists at 1/2 filling.

To reveal the mapping from Rydberg atom model to the long-range Ising model, we rewrite Eq. (1) in the main text in terms of spin operators. More precisely, by substituting $\hat{n}_i = \hat{S}_i^z + \frac{1}{2}\hat{I}$ into Eq. (1) in the main text we arrive at the following Hamiltonian:

$$\hat{H} = \sum_{i<j} U_{ij} \hat{S}_i^z \hat{S}_j^z + \sum_i h_i \hat{S}_i^z + \frac{\Omega}{2} \sum_i \hat{S}_i^x + \sum_{i<j} \frac{U_{ij}}{4} + \frac{N\delta}{2}, \quad (\text{B5})$$

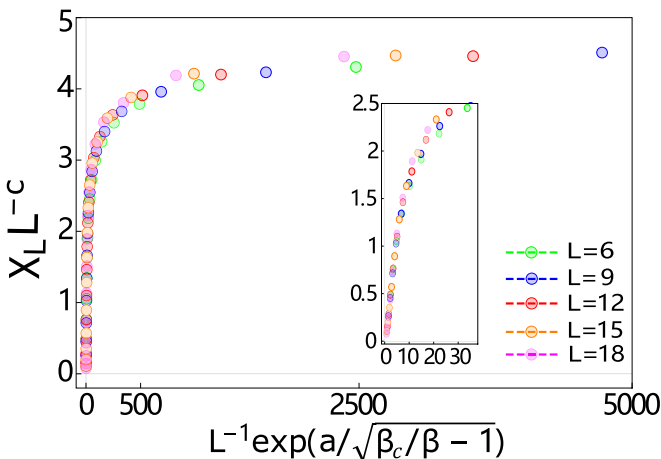


FIG. 15. The data collapse of TAF susceptibility from five sets of data $L/a = 6, 9, 12, 15, 18$, where the inset shows the fitting results in the range $L^{-1} e^{\frac{a}{\sqrt{\beta_c/\beta - 1}}} \in [0, 38]$.

where $h_i = \sum_{j \in \text{neighbor}} \frac{U_{ij}}{2} - \delta$ and N is the total number of lattice points. Here h_i is isotropic and when

$$\delta = \sum_{j \in \text{neighbor}} \frac{U_{ij}}{2}, \quad (\text{B6})$$

Eq. (B5) remains invariant under the transformation $\hat{S}_i^z \rightarrow -\hat{S}_i^z$, which is the particle-hole symmetry mentioned in the main text, that is, the system is Rydberg 1/2 filling in this case. As shown in Fig. 11, we consider the interaction between atoms to the seventh nearest neighbor and according to Eq. (B6), we can have

$$\begin{aligned} \delta &= \frac{1}{2} \times \left[\left(\frac{1.2}{1} \right)^6 \times 6 + \left(\frac{1.2}{\sqrt{3}} \right)^6 \times 6 + \left(\frac{1.2}{2} \right)^6 \times 6 \right. \\ &\quad + \left(\frac{1.2}{\sqrt{7}} \right)^6 \times 12 + \left(\frac{1.2}{3} \right)^6 \times 6 + \left(\frac{1.2}{2\sqrt{3}} \right)^6 \times 6 \\ &\quad \left. + \left(\frac{1.2}{\sqrt{13}} \right)^6 \times 12 \right] \\ &\approx 9.506, \end{aligned} \quad (\text{B7})$$

which is consistent with the numerical result of Fig. 1 in the main text.

Next, we provide more evidence for the $\sqrt{3} \times \sqrt{3}$ TAF phase mentioned in the main text that arises from an OBD mechanism at 1/2 filling, as shown in Fig. 12. In Figs. 12(a) and 12(b), order parameter m and static structure factor $S(\vec{Q})$ gradually decrease from a large value to a nonzero finite value with increasing size, which is consistent with the local minimum point at $\delta = 9.50\Omega$ in Figs. 2(a) and 2(b) in the main text. Similarly, from the inset in Fig. 12(d), we can see that the correlation length ratio $C(\vec{Q}, L)$ is also a local minimum at 1/2 filling, and it's clear that $C(\vec{Q}, L)$ increases as the size increases. In addition, for the Binder ratio given in Fig. 12(c), the results of different system sizes are close to 1, which also reflects the long-range order of the system. Therefore, combined with the results of Figs. 12(a) to 12(d), there is indeed a weak $\sqrt{3} \times \sqrt{3}$ TAF order at 1/2 filling. When δ has a proper deviation near 9.50Ω , the particle-hole symmetry will be broken so that the system will no longer have a KT phase transition. In the remainder of this subsection, we perform a finite-size scaling analysis to give a numerical verification for this point.

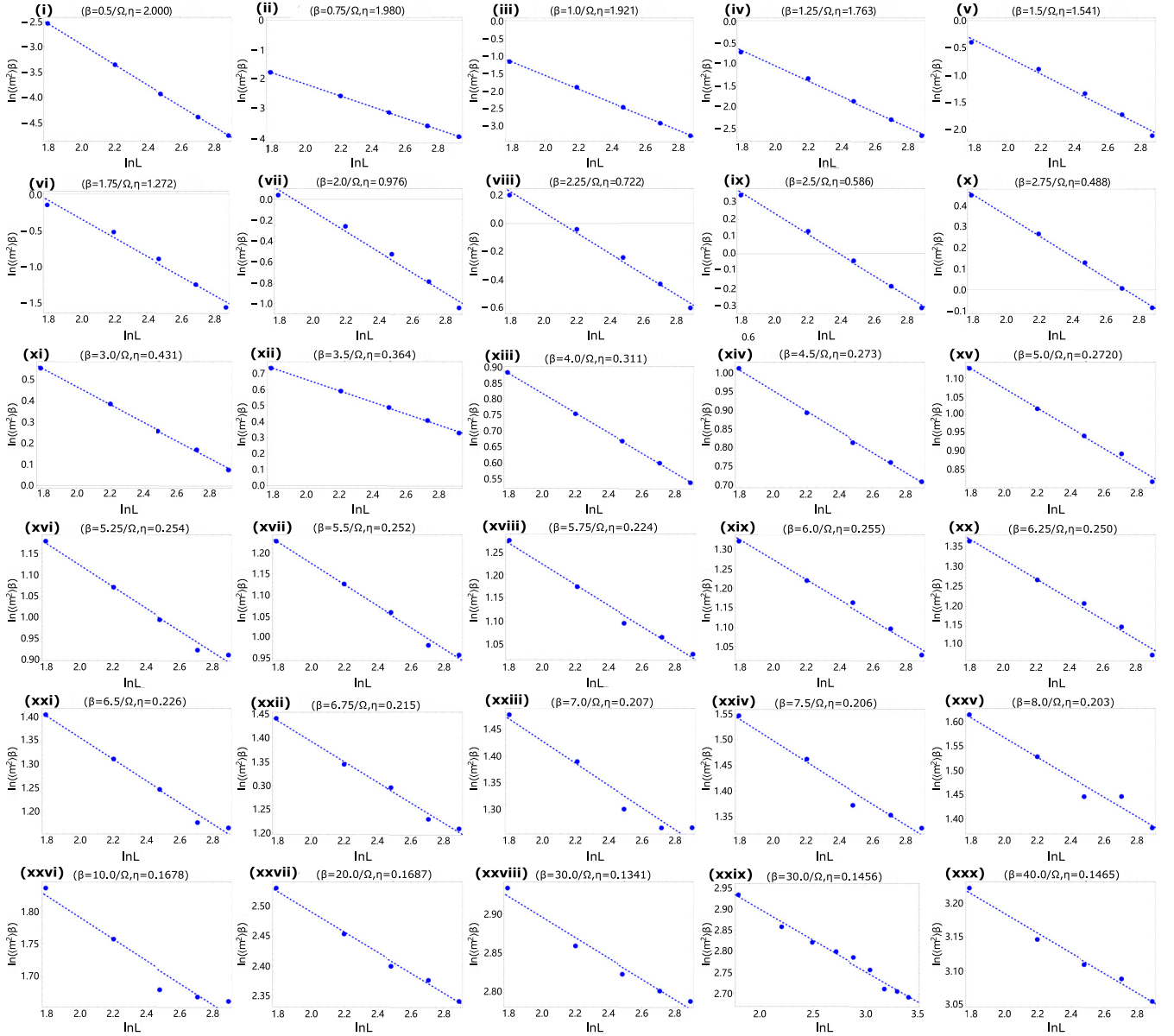


FIG. 16. The double logarithmic fitting of TAF susceptibility versus $\ln L$ at different temperatures, ranging from $\beta\Omega = 0.5$ to 40.0.

We choose $\delta = 9.3\Omega$, corresponding to the filling slightly deviating from $1/2$ filling, and investigate the nature of the TAF order parameter anisotropy. We calculate the Binder ratio U_B , C_6 , and C_3 with varying temperature as shown in Fig. 13. From the results of the Binder ratio in Fig. 13(a), as the inverse temperature is larger than $\beta_c = 3.0/\Omega$, the Binder ratio is close to 1, suggesting the TAF order is long range. The results of C_3 as shown in Fig. 13(c) demonstrate the TAF order is three-fold anisotropic as $\beta > 2.5/\Omega$. Hence, as the filling number slightly deviates from $1/2$ filling, the $U(1)$ isotropy of TAF order is not emergent at low temperature. We present the distribution histogram of the TAF order parameter upon fixing $\delta = 9.3\Omega$ with varying temperature in Figs. 14(a) to 14(c). With increasing temperature, the histogram of the TAF order evolves from the pattern with three-fold rotational symmetry to the single peak at zero associated with the disordered phase. Close to the transition temperature $\beta = 2.5/\Omega$, the

distribution histogram exhibits approximately $U(1)$ symmetry with tiny three-fold anisotropy. Because of the numerical uncertainty and finite-size effect, we cannot exclude the existence of an intermediate KT phase in a tiny temperature regime between low-temperature $\sqrt{3} \times \sqrt{3}$ TAF ordered phase and high-temperature disordered phase.

4. Additional results of KT transition

Figure 5(d) in the main text provides the results of data collapse analysis, giving rise to the critical temperature of the KT transition. In this subsection, we employ the same procedure of data collapse analysis using the data for $L/a = 6, 9, 12, 15, 18$ as shown in Fig. 15. The result of the KT transition is $\beta_c\Omega = 6.2507 \pm 0.4052$, consistent with the results obtained in the main text. In our analysis, the function $S = 1.7334$ in Fig. 5(d) of the main text and $S = 2.6589$

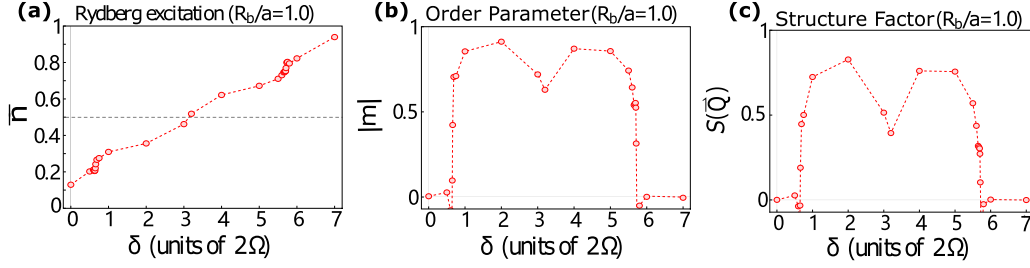


FIG. 17. (a) describes the Rydberg filling number as a function of δ . (b), (c) show the TAF order parameters and static structure factors, respectively. The Rydberg blockade radius is fixed at $R_b = 1.0a$.

in Fig. 15, indicating the excellent quality of data collapse. Hence, our simulation unambiguously reveals the TAF susceptibility obeys the scaling behavior of KT transition and the finite-temperature TAF transition occurring at $1/2$ filling belongs to the KT universality class.

Next, according to Eq. (B4), we perform a double logarithmic fitting for the TAF susceptibility and present the fitting results at 29 temperatures with $\delta = 9.50\Omega$, as shown in Fig. 16. At the KT-transition point, the accurate value of $\eta = 0.25$ is available. With increasing temperature, the fitted value of η gradually increases as clearly indicated in Fig. 16. In Fig. 16(xx), the critical exponent $\eta = 0.25$ when $\beta = 6.25/\Omega$, suggesting that the KT transition occurs at $\beta = 6.25/\Omega$ consistent with results obtained by data collapse. However, as the temperature further decreases, $\eta = 0.1341$ when $\beta = 30/\Omega$ as shown in Fig. 16(xxviii), which is greater than the lower critical exponent ($\eta = 1/9$) of the KT phase. To minimize the influence of finite size, we further increase the system size to $L = 30a$ and yield $\eta = 0.1456$, as shown in Fig. 16(xxix), indicating the lower-temperature bound of the KT phase is lower than $T = \Omega/30$. Therefore, compared with the previous results [82,88,94,107], we reach the conclusion that the long-range interaction substantially extends the temperature range of the KT phase.

APPENDIX C: QMC RESULTS FOR $R_b = 1.0a$

In this section, we present the numerical results for $R_b = 1.0a$, demonstrating that the main conclusions unveiled in the simulation of $R_b = 1.2a$ still hold. This section is organized as follows. In Appendix C 1, by calculating the order parameter m , the static structure factor $S(\vec{Q})$, Binder ratio U_B , and correlation length ratio $C(\vec{Q}, L)$, we access the ground-state phase diagram and confirm the existence of TAF order at $1/2$ filling.

In Appendix C 2 we plot the distribution histogram of the order parameters and the KT phase emerges at $1/2$ filling.

1. TAF phase and transition points

Figures 17(b) and 17(c) show the order parameter m and static structure factor $S(\vec{Q})$ with fixed $R_b = 1.0a$. Similarly, m and $S(\vec{Q})$ display two convexities at $1/3$ and $2/3$ filling, demonstrating the existence of $\sqrt{3} \times \sqrt{3}$ TAF long-range ordering. To further determine two transition points in Figs. 17(b) and 17(c), a finite-size scaling analysis is performed as shown in Fig. 18. From Fig. 18(a), the crossing points of the Binder ratio for different system sizes indicate the phase transition points $\delta/\Omega = 0.657 \pm 0.02$ and $5.712 \pm$

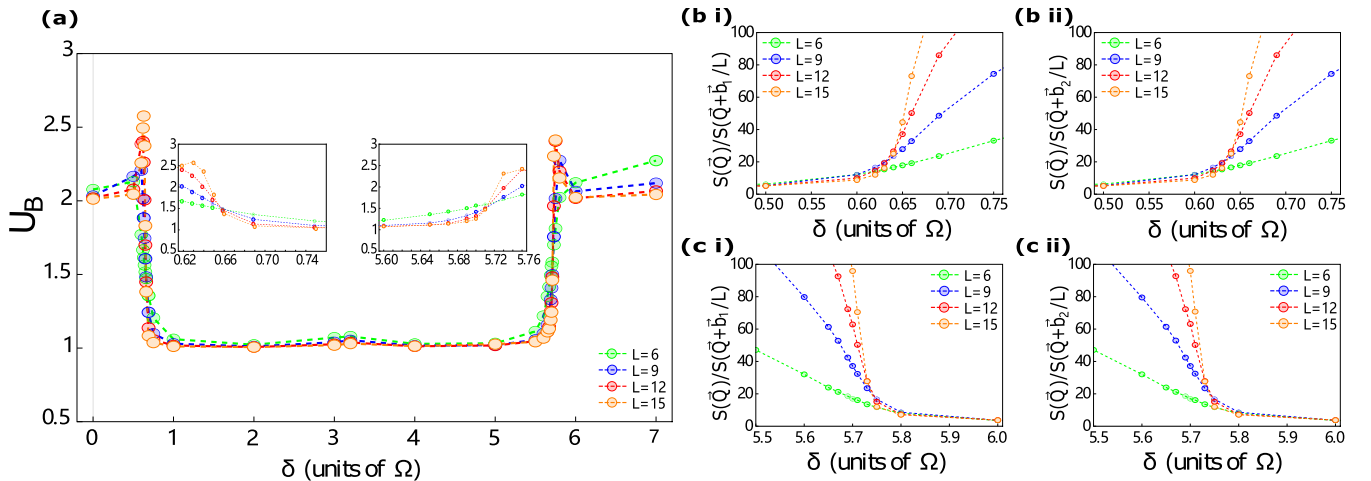


FIG. 18. (a) The overall trend of Binder ratio, where the insets are the zoomed-in view of the results in the vicinity of the transition points. (b), (c) indicate two transition points between disordered and TAF ordered phases at $1/3$ and $2/3$ fillings, respectively. Here, \vec{b}_1/L and \vec{b}_2/L denote two minimal lattice vectors in two directions on a two-dimensional lattice. Here, the linear system sizes in the simulation are $L/a = 6, 9, 12, 15$.

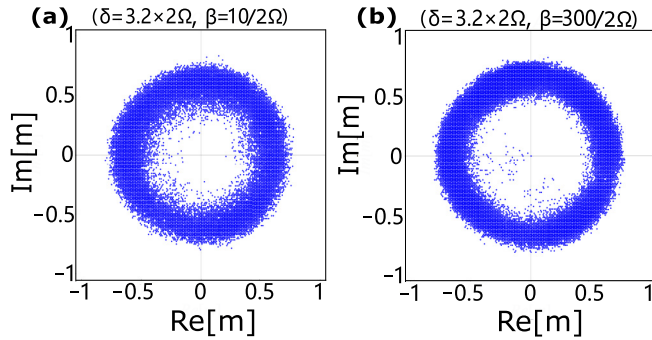


FIG. 19. The distribution histogram of TAF order parameter at half filling. The Rydberg blockade radius $R_b = 1.0a$ and linear system size $L = 15a$. The inverse temperature is (a) $\beta = 10/2\Omega$ and (b) $\beta = 300/2\Omega$, corresponding to the temperature in Rydberg-atom array experiment [3] $T = 2100$ nK and 70 nK, respectively.

0.02. In addition, the correlation length ratios close to the two transition points are given in Figs. 18(b) and 18(c). The phase transition points given by correlation length ratios

are approximately consistent with the ones from the Binder ratios.

Moreover, Fig. 17(a) indicates the detuning frequency corresponding to $1/2$ filling is approximate $\delta = 3.20 \times 2\Omega$. The order parameter and static structure factor in Figs. 17(b) and 17(c) reach a nonzero local minimum at this point. Therefore, for $R_b = 1.0a$, the ground state also possesses $\sqrt{3} \times \sqrt{3}$ TAF long-range order at $1/2$ filling, arising from the OBD mechanism. Thus, the ground-state phase diagram for $R_b = 1.0a$ is qualitatively the same as the one for $R_b = 1.2a$ as shown in the main text.

2. KT phase at low temperature

To verify the existence of KT phase at $1/2$ filling, the distribution histogram of order parameters is directly given in this subsection, as shown in Fig. 19. We can see that the order parameters are distributed on an isotropic circle in a large temperature regime, which is a manifestation of the emergent $U(1)$ symmetry. Therefore, the system with $R_b = 1.0a$ has KT phase, especially the distribution of 70 nK near zero temperature in Fig. 19(b), which leads us to believe that the KT phase can also exist at zero temperature.

-
- [1] L. Balents, *Nature (London)* **464**, 199 (2010).
- [2] Y. Zhou, K. Kanoda, and T.-K. Ng, *Rev. Mod. Phys.* **89**, 025003 (2017).
- [3] P. Scholl, M. Schuler, H. J. Williams, A. A. Eberharter, D. Barredo, K. N. Schymik, V. Lienhard, L. P. Henry, T. C. Lang, T. Lahaye, A. M. Lauchli, and A. Browaeys, *Nature (London)* **595**, 233 (2021).
- [4] S. Ebadi, T. T. Wang, H. Levine, A. Keesling, G. Semeghini, A. Omran, D. Bluvstein, R. Samajdar, H. Pichler, W. W. Ho, S. Choi, S. Sachdev, M. Greiner, V. Vuletic, and M. D. Lukin, *Nature (London)* **595**, 227 (2021).
- [5] G. Semeghini, H. Levine, A. Keesling, S. Ebadi, T. T. Wang, D. Bluvstein, R. Verresen, H. Pichler, M. Kalinowski, R. Samajdar, A. Omran, S. Sachdev, A. Vishwanath, M. Greiner, V. Vuletic, and M. D. Lukin, *Science* **374**, 1242 (2021).
- [6] D. Barredo, S. de Léséleuc, V. Lienhard, T. Lahaye, and A. Browaeys, *Science* **354**, 1021 (2016).
- [7] D. Barredo, V. Lienhard, S. de Léséleuc, T. Lahaye, and A. Browaeys, *Nature (London)* **561**, 79 (2018).
- [8] M. Endres, H. Bernien, A. Keesling, H. Levine, E. R. Anschuetz, A. Krajenbrink, C. Senko, V. Vuletic, M. Greiner, and M. D. Lukin, *Science* **354**, 1024 (2016).
- [9] I. Bloch, J. Dalibard, and S. Nascimbène, *Nat. Phys.* **8**, 267 (2012).
- [10] A. Gaëtan, Y. Miroshnychenko, T. Wilk, A. Chotia, M. Viteau, D. Compara, P. Pillet, A. Browaeys, and P. Grangier, *Nat. Phys.* **5**, 115 (2009).
- [11] C. Gross and I. Bloch, *Science* **357**, 995 (2017).
- [12] P. Schauß, M. Cheneau, M. Endres, T. Fukuhara, S. Hild, A. Omran, T. Pohl, C. Gross, S. Kuhr, and I. Bloch, *Nature (London)* **491**, 87 (2012).
- [13] E. Urban, T. A. Johnson, T. Henage, L. Isenhower, D. D. Yavuz, T. G. Walker, and M. Saffman, *Nat. Phys.* **5**, 110 (2009).
- [14] K.-N. Schymik, V. Lienhard, D. Barredo, P. Scholl, H. Williams, A. Browaeys, and T. Lahaye, *Phys. Rev. A* **102**, 063107 (2020).
- [15] V. Bharti, S. Sugawa, M. Mizoguchi, M. Kunimi, Y. Zhang, S. de Léséleuc, T. Tomita, T. Franz, M. Weidemüller, and K. Ohmori, *Phys. Rev. Lett.* **131**, 123201 (2023).
- [16] S. Hollerith, K. Srakaew, D. Wei, A. Rubio-Abadal, D. Adler, P. Weckesser, A. Kruckenhauser, V. Walther, R. van Bijnen, J. Rui, C. Gross, I. Bloch, and J. Zeiher, *Phys. Rev. Lett.* **128**, 113602 (2022).
- [17] D. Okuno, Y. Nakamura, T. Kusano, Y. Takasu, N. Takei, H. Konishi, and Y. Takahashi, *J. Phys. Soc. Jpn.* **91**, 084301 (2022).
- [18] K. Srakaew, P. Weckesser, S. Hollerith, D. Wei, D. Adler, I. Bloch, and J. Zeiher, *Nat. Phys.* **19**, 714 (2023).
- [19] Y. Q. Zou, M. Berngruber, V. S. V. Anasuri, N. Zuber, F. Meinert, R. Low, and T. Pfau, *Phys. Rev. Lett.* **130**, 023002 (2023).
- [20] P. Schauß, J. Zeiher, T. Fukuhara, S. Hild, M. Cheneau, T. Macrì, T. Pohl, I. Bloch, and C. Gross, *Science* **347**, 1455 (2015).
- [21] D. Barredo, H. Labuhn, S. Ravets, T. Lahaye, A. Browaeys, and C. S. Adams, *Phys. Rev. Lett.* **114**, 113002 (2015).
- [22] H. Labuhn, D. Barredo, S. Ravets, S. de Léséleuc, T. Macrì, T. Lahaye, and A. Browaeys, *Nature (London)* **534**, 667 (2016).
- [23] H. Bernien, S. Schwartz, A. Keesling, H. Levine, A. Omran, H. Pichler, S. Choi, A. S. Zibrov, M. Endres, M. Greiner, V. Vuletic, and M. D. Lukin, *Nature (London)* **551**, 579 (2017).
- [24] V. Lienhard, S. de Léséleuc, D. Barredo, T. Lahaye, A. Browaeys, M. Schuler, L.-P. Henry, and A. M. Läuchli, *Phys. Rev. X* **8**, 021070 (2018).
- [25] E. Guardado-Sanchez, P. T. Brown, D. Mitra, T. Devakul, D. A. Huse, P. Schauß, and W. S. Bakr, *Phys. Rev. X* **8**, 021069 (2018).

- [26] H. Kim, Y. J. Park, K. Kim, H. S. Sim, and J. Ahn, *Phys. Rev. Lett.* **120**, 180502 (2018).
- [27] A. Browaeys and T. Lahaye, *Nat. Phys.* **16**, 132 (2020).
- [28] S. de Léséleuc, V. Lienhard, P. Scholl, D. Barredo, S. Weber, N. Lang, H. Peter Büchler, T. Lahaye, and A. Browaeys, *Science* **365**, 775 (2019).
- [29] Y. Song, M. Kim, H. Hwang, W. Lee, and J. Ahn, *Phys. Rev. Res.* **3**, 013286 (2021).
- [30] R. Verresen, M. D. Lukin, and A. Vishwanath, *Phys. Rev. X* **11**, 031005 (2021).
- [31] M. Kornjača, R. Samajdar, T. Macrì, N. Gemelke, S.-T. Wang, and F. Liu, [arXiv:2211.00653](https://arxiv.org/abs/2211.00653).
- [32] M. Kalinowski, R. Samajdar, R. G. Melko, M. D. Lukin, S. Sachdev, and S. Choi, *Phys. Rev. B* **105**, 174417 (2022).
- [33] G.-Q. An, Y.-H. Zhou, T. Wang, and X.-F. Zhang, *Phys. Rev. B* **106**, 134506 (2022).
- [34] R. Samajdar, W. W. Ho, H. Pichler, M. D. Lukin, and S. Sachdev, *Phys. Rev. Lett.* **124**, 103601 (2020).
- [35] R. Samajdar, W. W. Ho, H. Pichler, M. D. Lukin, and S. Sachdev, *Proc. Natl. Acad. Sci.* **118**, e2015785118 (2021).
- [36] S. Fey, S. C. Kapfer, and K. P. Schmidt, *Phys. Rev. Lett.* **122**, 017203 (2019).
- [37] B. Yan, S. A. Moses, B. Gadway, J. P. Covey, K. R. A. Hazzard, A. M. Rey, D. S. Jin, and J. Ye, *Nature (London)* **501**, 521 (2013).
- [38] Y. L. Zhou, M. Ortner, and P. Rabl, *Phys. Rev. A* **84**, 052332 (2011).
- [39] D. Bluvstein, A. Omran, H. Levine, A. Keesling, G. Semeghini, S. Ebadi, T. T. Wang, A. A. Michailidis, N. Maskara, W. W. Ho, S. Choi, M. Serbyn, M. Greiner, V. Vuletić, and M. D. Lukin, *Science* **371**, 1355 (2021).
- [40] A. Mazurenko, C. S. Chiu, G. Ji, M. F. Parsons, M. Kanasz-Nagy, R. Schmidt, F. Grusdt, E. Demler, D. Greif, and M. Greiner, *Nature (London)* **545**, 462 (2017).
- [41] M. Morgado and S. Whitlock, *AVS Quantum Sci.* **3**, 023501 (2021).
- [42] J. Zeiher, J.-y. Choi, A. Rubio-Abadal, T. Pohl, R. van Bijnen, I. Bloch, and C. Gross, *Phys. Rev. X* **7**, 041063 (2017).
- [43] J. Zeiher, R. van Bijnen, P. Schauß, S. Hild, J.-y. Choi, T. Pohl, I. Bloch, and C. Gross, *Nat. Phys.* **12**, 1095 (2016).
- [44] C. Chen, G. Bornet, M. Bintz, G. Emperauger, L. Leclerc, V. S. Liu, P. Scholl, D. Barredo, J. Hauschild, S. Chatterjee, M. Schuler, A. M. Läuchli, M. P. Zaletel, T. Lahaye, N. Y. Yao, and A. Browaeys, *Nature (London)* **616**, 691 (2023).
- [45] A. F. Tzortzakakis, D. Petrosyan, M. Fleischhauer, and K. Mølmer, *Phys. Rev. A* **106**, 063302 (2022).
- [46] Z. Zhang, M. Yuan, B. Sundar, and K. R. A. Hazzard, [arXiv:2201.08463](https://arxiv.org/abs/2201.08463).
- [47] A. Kruckenhauser, R. van Bijnen, T. V. Zache, M. D. Liberto, and P. Zoller, *Quantum Sci. Technol.* **8**, 015020 (2023).
- [48] J. Y. Lee, J. Ramette, M. A. Metlitski, V. Vuletić, W. W. Ho, and S. Choi, *Phys. Rev. Lett.* **131**, 083601 (2023).
- [49] J. A. S. Lourenço, G. Higgins, C. Zhang, M. Hennrich, and T. Macrì, *Phys. Rev. A* **106**, 023309 (2022).
- [50] M. Sarkar, M. Pal, A. Sen, and K. Sengupta, *SciPost Phys.* **14**, 004 (2023).
- [51] P. Scholl, H. J. Williams, G. Bornet, F. Wallner, D. Barredo, L. Henriët, A. Signoles, C. Hainaut, T. Franz, S. Geier, A. Tebben, A. Salzinger, G. Zürn, T. Lahaye, M. Weidemüller, and A. Browaeys, *PRX Quantum* **3**, 0020303 (2022).
- [52] X. Wu, F. Yang, S. Yang, K. Mølmer, T. Pohl, M. K. Tey, and L. You, *Phys. Rev. Res.* **4**, L032046 (2022).
- [53] Z. Zhou, Z. Yan, C. Liu, Y. Chen, and X.-F. Zhang, [arXiv:2212.10863](https://arxiv.org/abs/2212.10863).
- [54] Z. Yan, Y.-C. Wang, R. Samajdar, S. Sachdev, and Z. Y. Meng, *Phys. Rev. Lett.* **130**, 206501 (2023).
- [55] Y. Cheng, C. Li, and H. Zhai, *New J. Phys.* **25**, 033010 (2023).
- [56] A. Keesling, A. Omran, H. Levine, H. Bernien, H. Pichler, S. Choi, R. Samajdar, S. Schwartz, P. Silvi, S. Sachdev, P. Zoller, M. Endres, M. Greiner, V. Vuletić, and M. D. Lukin, *Nature (London)* **568**, 207 (2019).
- [57] C. J. Turner, A. A. Michailidis, D. A. Abanin, M. Serbyn, and Z. Papić, *Nat. Phys.* **14**, 745 (2018).
- [58] N. E. Myerson-Jain, S. Yan, D. Weld, and C. Xu, *Phys. Rev. Lett.* **128**, 017601 (2022).
- [59] V. Lienhard, P. Scholl, S. Weber, D. Barredo, S. de Léséleuc, R. Bai, N. Lang, M. Fleischhauer, H. P. Büchler, T. Lahaye, and A. Browaeys, *Phys. Rev. X* **10**, 021031 (2020).
- [60] Y. Cheng, S. Liu, W. Zheng, P. Zhang, and H. Zhai, *PRX Quantum* **3**, 040317 (2022).
- [61] Y. Cheng and C. Li, *Phys. Rev. B* **107**, 094302 (2023).
- [62] E. Guardado-Sanchez, B. M. Spar, P. Schauss, R. Belyansky, J. T. Young, P. Bienias, A. V. Gorshkov, T. Iadecola, and W. S. Bakr, *Phys. Rev. X* **11**, 021036 (2021).
- [63] S. Ohler, M. Kiefer-Emmanouilidis, and M. Fleischhauer, *Phys. Rev. Res.* **5**, 013157 (2023).
- [64] Q. Chen, S. A. Chen, and Z. Zhu, *SciPost Phys.* **15**, 052 (2023).
- [65] C. J. Turner, J.-Y. Desautels, K. Bull, and Z. Papić, *Phys. Rev. X* **11**, 021021 (2021).
- [66] L. Pan and H. Zhai, *Phys. Rev. Res.* **4**, L032037 (2022).
- [67] T.-H. Yang, B.-Z. Wang, X.-C. Zhou, and X.-J. Liu, *Phys. Rev. A* **106**, L021101 (2022).
- [68] A. Celi, B. Vermersch, O. Viyuela, H. Pichler, M. D. Lukin, and P. Zoller, *Phys. Rev. X* **10**, 021057 (2020).
- [69] M. Barbier, H. Lütjeharms, and W. Hofstetter, *Phys. Rev. A* **105**, 013326 (2022).
- [70] P. Fromholz, M. Tsitsishvili, M. Votto, M. Dalmonte, A. Nersesyan, and T. Chanda, *Phys. Rev. B* **106**, 155411 (2022).
- [71] G. Giudice, F. M. Surace, H. Pichler, and G. Giudici, *Phys. Rev. B* **106**, 195155 (2022).
- [72] M. Kalinowski, N. Maskara, and M. D. Lukin, *Phys. Rev. X* **13**, 031008 (2023).
- [73] J. Lee, P. A. Volkov, B. J. DeSalvo, and J. H. Pixley, *Phys. Rev. A* **107**, 053307 (2023).
- [74] R. Samajdar, D. G. Joshi, Y. Teng, and S. Sachdev, *Phys. Rev. Lett.* **130**, 043601 (2023).
- [75] K. Slagle, D. Aasen, H. Pichler, R. S. K. Mong, P. Fendley, X. Chen, M. Endres, and J. Alicea, *Phys. Rev. B* **104**, 235109 (2021).
- [76] M. Tsitsishvili, T. Chanda, M. Votto, P. Fromholz, M. Dalmonte, and A. Nersesyan, *Phys. Rev. B* **105**, 155159 (2022).
- [77] X.-J. Yu, S. Yang, J.-B. Xu, and L. Xu, *Phys. Rev. B* **106**, 165124 (2022).
- [78] C. L. Henley, *Phys. Rev. Lett.* **62**, 2056 (1989).
- [79] A. V. Chubukov and T. Jolicoeur, *Phys. Rev. B* **46**, 11137 (1992).
- [80] A. Chubukov, *Phys. Rev. Lett.* **69**, 832 (1992).
- [81] R. Moessner, S. L. Sondhi, and P. Chandra, *Phys. Rev. Lett.* **84**, 4457 (2000).

- [82] R. Moessner and S. L. Sondhi, *Phys. Rev. B* **63**, 224401 (2001).
- [83] J.-S. Bernier, M. J. Lawler, and Y. B. Kim, *Phys. Rev. Lett.* **101**, 047201 (2008).
- [84] E. Sela, H.-C. Jiang, M. H. Gerlach, and S. Trebst, *Phys. Rev. B* **90**, 035113 (2014).
- [85] M. Yue, Z. Wang, B. Mukherjee, and Z. Cai, *Phys. Rev. B* **103**, L201113 (2021).
- [86] A. G. Green, G. Conduit, and F. Krüger, *Annu. Rev. Condens. Matter Phys.* **9**, 59 (2018).
- [87] R. G. Melko, A. Paramekanti, A. A. Burkov, A. Vishwanath, D. N. Sheng, and L. Balents, *Phys. Rev. Lett.* **95**, 127207 (2005).
- [88] C. Liu, C.-J. Huang, and G. Chen, *Phys. Rev. Res.* **2**, 043013 (2020).
- [89] A. W. Sandvik, *Phys. Rev. E* **68**, 056701 (2003).
- [90] K. Damle, *Phys. Rev. Lett.* **115**, 127204 (2015).
- [91] Z. Hu, Z. Ma, Y.-D. Liao, H. Li, C. Ma, Y. Cui, Y. Shangguan, Z. Huang, Y. Qi, W. Li, Z. Y. Meng, J. Wen, and W. Yu, *Nat. Commun.* **11**, 5631 (2020).
- [92] H. Li, Y. D. Liao, B.-B. Chen, X.-T. Zeng, X.-L. Sheng, Y. Qi, Z. Y. Meng, and W. Li, *Nat. Commun.* **11**, 1111 (2020).
- [93] Y. Wang, S. Humeniuk, and Y. Wan, *Phys. Rev. B* **101**, 134414 (2020).
- [94] Y. D. Liao, H. Li, Z. Yan, H.-T. Wei, W. Li, Y. Qi, and Z. Y. Meng, *Phys. Rev. B* **103**, 104416 (2021).
- [95] Z. Dun, M. Daum, R. Baral, H. E. Fischer, H. Cao, Y. Liu, M. B. Stone, J. A. Rodriguez-Rivera, E. S. Choi, Q. Huang, H. Zhou, M. Mourigal, and B. A. Frandsen, *Phys. Rev. B* **103**, 064424 (2021).
- [96] A. W. Sandvik, *Phys. Rev. B* **59**, R14157(R) (1999).
- [97] A. W. Sandvik, A. Avella, and F. Mancini, *AIP Conf. Proc.* **1297**, 135 (2010).
- [98] E. Merali, I. J. De Vlugt, and R. G. Melko, [arXiv:2107.00766](https://arxiv.org/abs/2107.00766).
- [99] J. M. Kosterlitz and D. J. Thouless, *J. Phys. C* **6**, 1181 (1973).
- [100] Z.-X. Li and H. Yao, *Annu. Rev. Condens. Matter Phys.* **10**, 337 (2019).
- [101] Z.-X. Li, Y.-F. Jiang, and H. Yao, *Phys. Rev. Lett.* **117**, 267002 (2016).
- [102] Z. C. Wei, C. Wu, Y. Li, S. Zhang, and T. Xiang, *Phys. Rev. Lett.* **116**, 250601 (2016).
- [103] L. Wang, Y.-H. Liu, M. Iazzi, M. Troyer, and G. Harcos, *Phys. Rev. Lett.* **115**, 250601 (2015).
- [104] Z.-X. Li, Y.-F. Jiang, and H. Yao, *Phys. Rev. B* **91**, 241117(R) (2015).
- [105] K. Binder, *Z. Phys. B* **43**, 119 (1981).
- [106] M. S. S. Challa and D. P. Landau, *Phys. Rev. B* **33**, 437 (1986).
- [107] S. V. Isakov and R. Moessner, *Phys. Rev. B* **68**, 104409 (2003).
- [108] D. Blankschtein, M. Ma, A. N. Berker, G. S. Grest, and C. M. Soukoulis, *Phys. Rev. B* **29**, 5250 (1984).
- [109] J. M. Kosterlitz, *J. Phys. C: Solid State Phys.* **7**, 1046 (1974).
- [110] J. V. José, L. P. Kadanoff, S. Kirkpatrick, and D. R. Nelson, *Phys. Rev. B* **16**, 1217 (1977).
- [111] J. Houdayer and A. K. Hartmann, *Phys. Rev. B* **70**, 014418 (2004).
- [112] N. Kawashima and N. Ito, *J. Phys. Soc. Jpn.* **62**, 435 (1993).